Journal of Materials Chemistry C

Origin and Control of Room Temperature Ferromagnetism in Co,Zn-doped SnO_2: Oxygen Vacancies and their Local Environment

Journal:	*Journal of Materials Chemistry C*
Manuscript ID	TC-ART-12-2019-006830.R1
Article Type:	Paper
Date Submitted by the Author:	21-Feb-2020
Complete List of Authors:	Ho, Josha; University of Saskatchewan, Physics and Engineering Physics de Boer, Tristan; University of Saskatchewan, Physics and Engineering Physics Braun, Patrick; University of Saskatchewan, Physics and Engineering Physics Leedahl, Brett; University of Saskatchewan, Department of Physics and Engineering Physics Dhamodaran, Manikandan ; Pondicherry University, Physics Ramaswamy, Murugan; Pondicherry University, Physics Moewes, Alexander; University of Saskatchewan, Physics and Engineering Physics

Journal Name

ARTICLE TYPE

Cite this: DOI: 00.0000/xxxxxxxxxx

Origin and Control of Room Temperature Ferromagnetism in Co,Zn-doped SnO_2: Oxygen Vacancies and their Local Environment[†]

Josha Ho,[a] Tristan de Boer,[a‡] Patrick M. Braun,[a] Brett Leedahl,[a] Dhamodaran Manikandan,[b] Ramaswamy Murugan,[b] and Alexander Moewes[a]

Received Date
Accepted Date

DOI: 00.0000/xxxxxxxxxx

We combine quantitative x-ray spectroscopy and crystal field calculations to study Co and Zn co-doped SnO_2 dilute magnetic semiconductor systems, report the location of vacancies, and the new effect of vacancy transfer resulting in optical luminescence only present after annealing. We connect this phenomenon to mid gap states using the band structure of the material obtained via density functional theory. Furthermore, we give a new understanding of the interaction of transition metals within co-doped systems. Finally, we present new evidence that the ferromagnetism is mediated by the oxygen vacancies and the particular local environment of the vacancies can be controlled via the synthesis conditions.

1 Introduction

Spin electronics, or *spintronics* relies on detecting and manipulating electron spin in addition to electron charge.[1] The movement and orientation of spin, like the flow of electron charge, could be used to convey information, creating devices that are smaller, faster, and consume less energy than current solutions.[2] Attractive candidates for spintronic materials include dilute magnetic semiconductors (DMSs), where transition metal (TM) impurities are introduced into a semiconductor host lattice to induce magnetic properties in an otherwise non-magnetic semiconductor.[3] For real-world spintronic devices, a DMS should demonstrate ferromagnetic properties at and far above room temperature (~ 300 K).

Tin Oxide (SnO_2) has garnered a significant amount of interest in these applications as a semiconductor with a large band gap (~ 3.6 eV), relatively low cost, and nontoxicity. Some studies on TM-doped tin oxide have been performed and room temperature ferromagnetism (RTFM) has been reported with both ferromagnetic and non-ferromagnetic dopants.[4–6] To move forward with this promising material, it is crucial to understand the effect of various dopants on the host material. It has been suggested that the RTFM in TM-doped SnO_2 is related to oxygen vacancies.[7] Oxygen vacancies are a specific defect state in DMS systems, and have been shown to be affected by synthesis conditions; one of the major contributors to the defect state of these systems can be the annealing temperature which can improve the crystallinity of a material and the diffusion of dopants within a lattice.[8] Past investigations of doped SnO_2 reveal that at higher concentrations of dopants, materials can lose their magnetic properties, possibly due to a disordering caused by dopants on the host structure, or dopant clustering.[9]

Synchrotron-based spectroscopy techniques have been used to investigate TM-doped SnO_2 with both ferromagnetic and non-ferromagnetic dopants (Zn, Co, Cr, Fe, Ni) including co-doped iron and nickel primarily using x-ray absorption near-edge structure (XANES) and extended x-ray absorption fine structure (EXAFS) techniques.[10–13] In samples with zinc, cobalt, iron, and nickel dopants, oxygen vacancies are reported adjacent to substitutional dopant sites where trapped electrons compensate for the charge difference between dopants and the displaced Sn^{4+}. In the case of chromium substitution, Cr^{4+} ions cause a decrease in inherent oxygen vacancies in nanoscale SnO_2.[11]

Investigations of zinc–doped SnO_2 show significant changes in ferromagnetic properties as concentrations increase ($\sim 3\%$).[9] Co-doping can in general be efficient for increasing the dopant solubility, lowering the ionization energy of acceptors and donors, and increasing carrier mobility. Given the sensitivity of the overall magnetic properties of DMS systems to not just the concentration of dopants but also their local environments, it is important to understand how the the local environment of dopants and corresponding changes in the magnetic properties are affected by the synthesis conditions.[14]

In this paper, we will examine SnO_2 nanoparticles co-doped

---

[a] *Department of Physics and Engineering Physics, University of Saskatchewan, 116 Science Pl, Saskatoon, Saskatchewan, Canada. Fax: (306) 966-6400; Tel: (306) 966-6431; E-mail: tristan.deboer@usask.ca*
[b] *Department of Physics, Pondicherry University, Puducherry 605 014, India.*

with varying concentrations of both zinc and cobalt to investigate distortions to the SnO_2 lattice due to the introduction of two dissimilar dopants. The introduction of these two dopants creates the opportunity for two distinct dopant sites within the lattice and the investigation of the local distortions caused by each.

We present direct evidence for successful incorporation of both dopants together into an SnO_2 host using x-ray absorption spectroscopy (XAS), resonant x-ray emission spectroscopy (RXES), and x-ray excited optical luminescence (XEOL) measurements. Furthermore, via crystal field modeling we link this luminescence with the oxygen vacancies adjacent to dopant sites and attribute distinct luminescence values to specific dopants within the material. This allows a rigorous and complete picture on the effect of two dissimilar dopants on the structural properties which can then be connected to the magnetic properties of the overall material. This work does not address the exchange-coupling origin of ferromagnetism. Rather, it determines that ferromagnetism is present for particular local environments around the dopant atoms, and that this is the structural origin (rather than exchange-coupling origin) of the ferromagnetism.

2 Experiment and Theory

Undoped SnO_2, $Sn_{0.95}Co_{0.025}Zn_{0.025}O_2$, $Sn_{0.90}Co_{0.05}Zn_{0.05}O_2$, and $Sn_{0.85}Co_{0.075}Zn_{0.075}O_2$ were prepared by the hydrothermal method; detailed information regarding the synthesis of these materials can be found in a previous publication[15]. Following synthesis, a set of samples was annealed at 800°C for two hours in an air atmosphere. These are referred to as the "annealed" samples herein, compared to the "as-synthesized" samples. Both the as-synthesized and annealed samples exhibited RTFM, with the saturation magnetization for each sample shown in Table 1.

The RXES and XAS measurements probe the occupied and unoccupied density of states of a material, respectively. RXES records the emission resulting from decay from occupied states to fill core holes and the XAS monitors the excitation of core electrons into unoccupied states, thereby directly probing the occupied and unoccupied partial density of states, respectively. XAS measurements were taken on the REIXS beamline at the Canadian Light Source (CLS), with a resolving power $E/\Delta E = 5000$; this was measured using a silicon drift detector for partial florescence yield detection.[20] RXES measurements for cobalt were taken on Beamline 8.0.1 at the Advanced Light Source with a resolving power of 2000.[20,21]

X-ray excited optical luminescence (XEOL), an x-ray photon-in, optical photon-out process, monitors the optical transitions resulting from electron-hole recombinations of the excited core electrons. These measurements were performed at the SGM beamline at the Canadian Light Source (CLS) using a Ocean Optics QE 65000 spectrophotometer.[22]

The physical and electronic structure of defected and pristine SnO_2 was modeled using density functional theory (DFT) with WIEN2k, a full-potential, all electron code, which uses linearized augmented plane waves in a Kohn-Sham scheme[23]. The PBEsol exchange-correlation functional, a generalized gradient approximation (GGA) functional formulated to optimize the properties of densely packed solids was used to perform the calculations.[24] This particular functional was used because it shown to well describe the structural properties of both semiconductors[25] and 3d transition metals.[26] An $RK_{max} = 8.0$ was used with a k-mesh selected so that the total energy was stable to within 10^{-5} Ry. This resulted in a k-mesh of $10 \times 10 \times 14$ for the unit cell of SnO_2. The lattice parameters for SnO_2 are based on the neutron diffraction determined lattice.[27] For calculations involving dopants and vacancies, these defects were added to a $2 \times 2 \times 2$ SnO_2 supercell, with a correspondingly smaller k-mesh. For each calculation, the atomic positions are allowed to relax while holding the lattice parameters constant. The DFT calculations are also used to calculate the electronic band structure as well as the Zn L-edge XAS spectra, allowing for a detailed comparison with experiment. These spectra are calculated by multiplying the partial density of states with a dipole transition matrix and radial transition probability.[28] All of the band structure diagrams are shown for a path in the Brillouin zone for the single unit cell of SnO_2.[29] For supercell calculations, points in the supercell Brillouin zone have been mapped to the original unit cell representation using a Bloch spectral density approach.[30]

Due to the strong electron-electron correlation effects of the $3d$ electrons, cobalt spectra are modeled more accurately by considering multiplet effects.[31] The Co $L_{2,3}$ RXES and XAS spectra are modeled using crystal field multiplet calculations in the approach originally formulated by Cowan.[32] The Quanty full multiplet code was utilized in two methodologies.[33] Firstly, crystal field parameters resulting from d orbital energy splitting can be used to describe the local coordination of the Co atoms and understand the overall lattice structure surrounding the dopant atom, matching results from experiment. Secondly, supercells obtained through relaxing structures with implanted dopants via DFT are used to generate the Madelung potentials of the crystal structure using an Ewald summation over point charges and the subsequent potentials are used to model the spectra via the same multiplet-based crystal field calculations.[34]

3 Results and Discussion

3.1 Co $L_{2,3}$ XAS and RXES

3.1.1 As-Synthesized $Sn_{0.85}Co_{0.075}Zn_{0.075}O_2$

We begin by considering the sample with the highest concentration of dopants, as-synthesized $Sn_{0.85}Co_{0.075}Zn_{0.075}O_2$. Examining first the as-synthesized case and in the following section after an annealing process, we isolate the effect that annealing has on the properties of the material.

This as-synthesized sample is first examined via Co $L_{2,3}$ RXES and XAS (Fig. 1), allowing the investigation of the excitations for the $2p$ orbitals to the unoccupied conduction band states. The experimental spectra are displayed on an energy loss scale (red in Fig. 1), along with two theoretical models (green and orange in Fig. 1), matching both the characteristics of the absorption spectra and the emission spectra at two incident energies (labeled A and B in Fig. 1), providing insight into the d–d transitions resulting from reordering of electrons within the $3d$ orbitals. Because of this, the emission spectra prove vital in understanding the structural defects around the dopants. The as-synthesized

Table 1 Saturation magnetization (M_S) of the samples studied in this work measured at 300 K (adapted from Ref. 15.) and comparison with previous reported values of a similar DMS materials.

Investigated systems in this work			Literature reports		
Samples	As-synthesized M_S 10^{-3} emu/g	Annealed M_S 10^{-3} emu/g	Samples	M_S 10^{-3} emu/g	References
Undoped SnO2	Diamagnetic	7.4	SnO2	0.2	16
$Sn_{0.95}Co_{0.025}Zn_{0.025}O_2$	7.5	10.2	$Sn_{0.94}Co_{0.03}Zn_{0.02}O_2$	0.7	17
			$Sn_{0.95}Co_{0.03}Zn_{0.02}O_2$	1.4	17
$Sn_{0.90}Co_{0.050}Zn_{0.050}O_2$	33.1	20.9	$Sn_{0.90}Co_{0.05}Zn_{0.05}O_2$	0.9	18
			$Sn_{0.96}Co_{0.03}Zn_{0.01}O_2$	3	19
$Sn_{0.85}Co_{0.075}Zn_{0.075}O_2$	55	49	$Sn_{0.92}Co_{0.03}Zn_{0.05}O_2$	1.9	18
			$Sn_{0.94}Co_{0.010}Zn_{0.05}O_2$	0.2	18

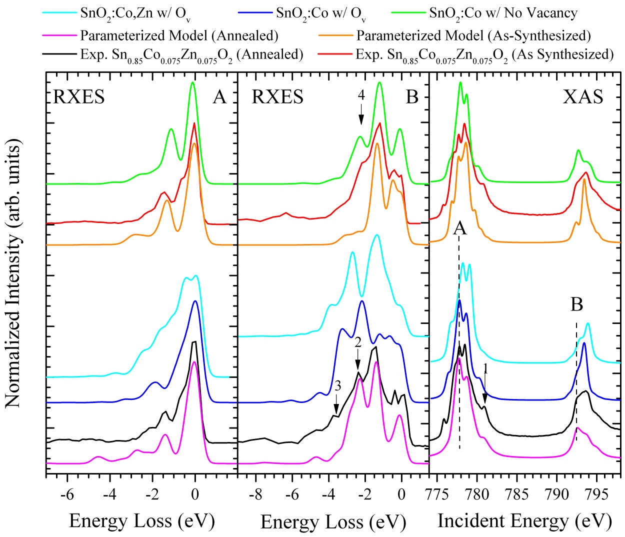

Fig. 1 Comparison of experimental XAS (right) and RXES (left and center) spectra for as-synthesized (red) and annealed (black) $Sn_{0.85}Co_{0.075}Zn_{0.075}O_2$ to calculations. Parameterized models (orange for as-synthesized, magenta for annealed) indicates a distorted tetragonal coordination. Spectra calculated from DFT structural models including SnO_2 doped with Co, SnO_2 doped with Co and a Co-adjacent O vacancy, and SnO_2 doped with Co and Zn and a Co-adjacent O vacancy are shown in green, dark blue, and light blue, respectively.

$Sn_{0.85}Co_{0.075}Zn_{0.075}O_2$ spectra are investigated (red in Fig. 1) in relation to two theoretical models produced via multiplet calculations. Firstly, the "parameterized model" (orange in Fig. 1) is found through fitting calculated spectra to experiment by adjusting crystal field splitting values. The agreement between these calculated and experimental spectra is prevalent in the RXES spectra (left and centre panels in Fig. 1). Firstly in the location of the two main features in the L_2 emission (centre panel) at -1.2 eV and -2.3 eV; secondly, in the location of the strong peak in the L_3 emission (left at -1.6 eV). These calculated spectra have crystal field parameters $10Dq = -1.60$, $Ds = -0.10$, $Dt = -0.200$ and Slater integral scalings of $F_{dd} = 0.700$, $F_{pd} = 0.700$ and $G_{pd} = 0.700$ and the atomic spin-orbit coupling constant ζ_{2p} was scaled by a factor of 1.000. These parameters deviate from the nominal values of $Ds = 0$, $Dt = 0$, and a positive $10Dq$ of an octahedral coordination due to the local environment of the atom and any distortions occurring. This provides a fundamental insight into the bonding process, which in this case, yields a highly distorted tetrahedral structure, as indicated by negative $10Dq$ and relatively large Ds and Dt values.

In addition to this parameterized model, we model the material by the construction of structural models of $Co^{2+} \rightarrow Sn^{4+}$ substitution (green), $Co^{2+} \rightarrow Sn^{4+}$ substitution with an adjacent oxygen vacancy to the substitution (dark blue), and $Co^{2+}, Zn^{2+} \rightarrow Sn^{4+}$ substitution with an oxygen vacancy adjacent to the cobalt site (light blue) were constructed, and relaxed using DFT (Fig. 2). This insertion of an oxygen vacancy follows the results of SnO_2 singly doped with Co, and allows trapped electrons to compensate for the valency difference between Co^{2+} and Sn^{4+}.[35] Comparing all three models to the as-synthesized $Sn_{0.85}Co_{0.075}Zn_{0.075}O_2$ experimental spectra, the $Co^{2+} \rightarrow Sn^{4+}$ substitution with no oxygen vacancy (green in Fig. 1) provides the best agreement with the experimental spectra, primarily in the location of a low energy-loss feature (labeled 4 in Fig. 1) matching the experimentally found shoulder due to dd-energy losses. This demonstrates the absence of oxygen vacancies within the as-synthesized $Sn_{0.85}Co_{0.075}Zn_{0.075}O_2$ sample, ruling out oxygen vacancies as the cause behind the structural distortions identified in the parameterized model. In the case of $Co^{2+}, Zn^{2+} \rightarrow Sn^{4+}$ substitution with an oxygen vacancy adjacent to the cobalt site, various separations of the Co and Zn atoms were considered. It was found that the lowest energy cell was obtained when the Co and Zn dopant atoms were maximally separated, and this is the model presented in Fig. 2. This suggests that, growth conditions permitting, these co-dopants prefer to be well separated.

The usage of two theoretical models with distinct methodologies allow the extraction of key real-world properties. More specifically, the "parameterized model" (orange in Fig. 1) is found through fitting calculated spectra to experiment by adjusting crystal field splitting values. These parameters describe the relative energies of the d orbitals of the atom and any distortions occurring, and provide a fundamental insight into the local coordination. The structural model includes dopant cobalt atoms placed within a host SnO_2 lattice with and without oxygen vacancies adjacent to the cobalt atoms (vacancy sites were seen to be equiva-

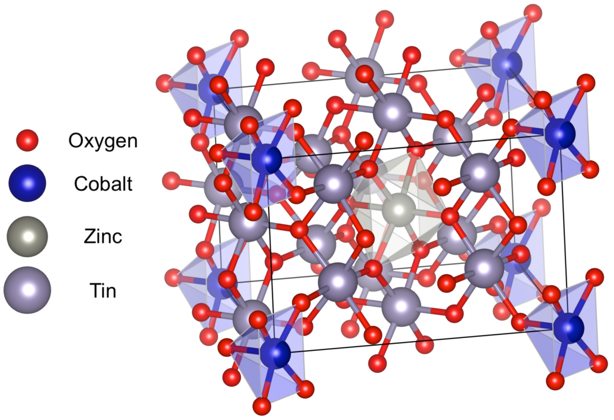

Fig. 2 Relaxed coordination of cobalt substitution into host SnO_2 material without oxygen vacancy (upper-left), with oxygen vacancy (bottom-left), and zinc and cobalt with a vacancy adjacent to the cobalt relaxed in a $2\times2\times2$ SnO_2 crystal structure. The relaxed structures show warping of the tetragonal coordination around the dopant atoms substituted into the lattice. Polyhedra are shown around the dopant atoms.

lent around the dopant atoms), and relaxed via DFT. These two methodologies work in conjunction to both understand the bonding and the role of oxygen vacancies in this bonding.

3.1.2 Annealed $Sn_{0.85}Co_{0.075}Zn_{0.075}O_2$

Samples that were annealed at 800°C for two hours were measured in the same methodology as the "as-synthesized" samples above. By investigating samples with the same dopant concentration, this isolates the effects of annealing and the usage of the same theoretical modelling as above to understand molecular changes resulting from the annealing. Mirroring our analysis of the as-sythesized case, we consider the experimental Co L-edge emission and absorption spectra of annealed $Sn_{0.85}Co_{0.075}Zn_{0.075}O_2$ as shown in black in Fig. 1 alongside three theoretical models. The crystal field parameters of the annealed spectra are $10Dq = -0.360$, $Ds = -0.380$, $Dt = -0.429$ and Slater integral scalings of $F_{dd} = 0.324$, $F_{pd} = 0.530$ and $G_{pd} = 0.675$ and the atomic spin-orbit coupling constant ζ_{2p} was scaled by a factor of 1.052. In comparison to the as-synthesized case, the strong negative $10Dq$ value demonstrates the increase in bond strength of the cobalt ion to the adjacent oxygen compared to the as-synthesized case. The decrease in magnitude of the Ds value indicates less distortion in the tetragonal structure, confirming the expected relaxation of the Co^{2+} substitution into the SnO_2 lattice resulting from the annealing process.

In addition to the parameterized model, we compare the experimentally obtained spectra with the three structural models described above in Section 3.1.1 ($Co^{2+} \rightarrow Sn^{4+}$ substitution, $Co^{2+} \rightarrow Sn^{4+}$ substitution with an adjacent oxygen vacancy to the substitution, and $Co^{2+},Zn^{2+} \rightarrow Sn^{4+}$ substitution with an oxygen vacancy adjacent to the cobalt site).

With as-synthesized samples, the measurement of features at low energy loss values leads to agreement with a substitutional cobalt model with no vacancy (green in Fig. 1). In contrast, for the annealed samples, good agreement is obtained between experiment and theory with a substitutional cobalt model with an adjacent oxygen vacancy (dark blue in Fig. 1). Considering a model in which a substitutional Zn atom is included, shown in Fig. 2, moderate but worse agreement is obtained. This suggests that, for this level of theory, the local environment of Co is best modelled without considering the presence of co-dopants.

Once again, two distinct methodologies allow the extraction of not only the local structure of the dopants, but also the cause of the distortions, in this case the oxygen vacancies compounding upon the distortions seen with the cobalt dopant substitution. This gives a clear picture of the absence of cobalt-adjacent oxygen vacancies in the as-synthesized samples and the existence of cobalt-adjacent oxygen vacancies in the annealed samples.

We note that, for both the annealed and as-synthesized samples, the differences between experimentally measured spectra of samples with varying cobalt and zinc concentrations are less than the difference between the best fitting models in both those yielding crystal field splitting parameters and those generated using relaxed structural models. This suggests that for both the annealed and as-synthesized samples, in the range of dopant concentrations considered in this work, the overall local environment of the Co atoms varies negligibly.

3.2 Zn $L_{2,3}$-edge XAS measurements

Fig. 3 displays Zn $L_{2,3}$ XAS spectra of both annealed and as-grown samples. Also shown are the second derivative of annealed and as-grown Zn $L_{2,3}$ XAS spectra, the first inflection point giving a graphical comparison of the absorption edge onset.[36]

Calculated XAS spectra, generated using the same DFT relaxed structures during cobalt L-edge modeling, can be compared to experimental results. As-synthesized samples show good agreement with a Zn^{2+}–Sn^{4+} model with an oxygen vacancy adjacent to the Zn^{2+} site. In addition, the energy shift seen in the onset of the annealed samples shows agreement with a Co^{2+},Zn^{2+}–Sn^{4+} model with a vacancy adjacent to the Co^{2+} site seen in Fig. 3 (magenta). This displays the positioning of oxygen vacancies adjacent to zinc atoms in as-synthesized samples and, with conjunction with our cobalt $L_{2,3}$ XAS and RXES measurements, demonstrates their movement to positioning adjacent to cobalt atoms after annealing.

Similar to our investigation in the cobalt case, the differences between experimentally measured spectra of samples with varying cobalt and zinc concentrations are less than the difference between the best fitting model and the experimental spectra.

3.3 The connection of oxygen vacancies positioning to magnetic properties

With the observation of the oxygen vacancy migration from zinc adjacent sites to cobalt adjacent sites as a result of an annealing process, we connect this to the magnetic properties of the material to understand the effects of oxygen vacancies on the magnetic properties of the material.

Considering Table 1, at low concentrations of Co and Zn co-doping, enhanced magnetization has been observed in the annealed samples compared to the as-synthesized samples. We also note that, although the saturation magnetization (M_S) increases

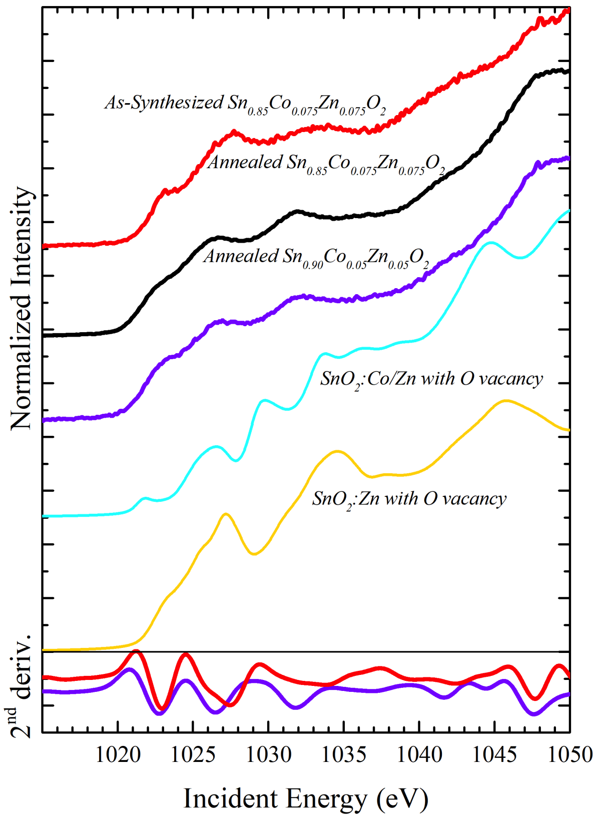

Fig. 3 Zn $L_{2,3}$ XAS spectra of annealed SnO_2 samples (black and violet) with as-synthesized $Sn_{0.85}Co_{0.075}Zn_{0.075}O_2$ (red), second derivative for $Sn_{0.90}Co_{0.05}Zn_{0.05}O_2$ and as-synthesized $Sn_{0.85}Co_{0.075}Zn_{0.075}O_2$ shown at the bottom, and DFT models in cyan and yellow. In the second derivative, the decrease in onset energy between the "as-synthesized" and the annealed samples is clear, showing the shift from zinc adjacent oxygen vacancies to cobalt adjacent oxygen vacancies.

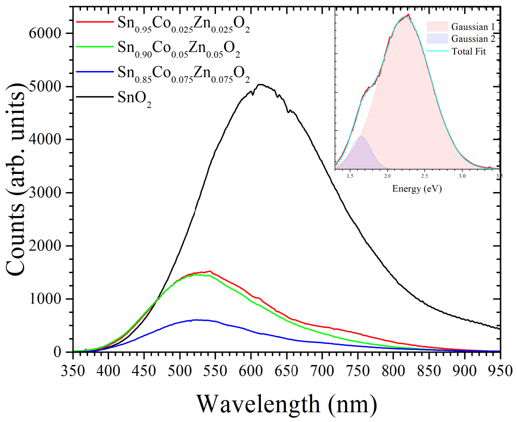

Fig. 4 XEOL spectra for annealed SnO_2 samples. Undoped SnO_2 (black) is seen with a single peak at ~ 640 nm, and doped SnO_2 consistently show a feature centered at 550 nm. A second feature is visible in the $Sn_{0.95}Co_{0.025}Zn_{0.075}O_2$ (red) at 750 nm. This clearly shows the shift of mid-gap defects from the inherent SnO_2 oxygen vacancies to a defect caused by TM doping. Gaussian fitting for the features is shown on an energy scale in the inset.

with increasing dopant concentration for each set of samples, at high dopant concentrations, the observed M_S decreases with annealing. Prior work suggests this is due to the increasing importance of antiferromagnetic interactions.[15] While our XAS and RXES techniques do not address the concentration of oxygen vacancies, the migration of these oxygen vacancies upon annealing can be linked to this enhanced saturation magnetism. To further investigate the the oxygen vacancies, the luminescence for samples with varying dopant concentrations can be examined.

3.4 X-ray excited optical luminescence (XEOL)

X-ray excited optical luminescence (XEOL) measurements, which are complimentary to XAS in investigating the effect of dopants on the band structure of a material, were performed on our SnO_2 samples and are shown in Fig. 4. The as-synthesized samples are not shown as they display no observable luminescence. The nanoscale undoped annealed SnO_2 presents a strong resolved peak at ~640 nm (1.93 eV), agreeing with previous results for nanoscale SnO_2.[37] Considering our doped annealed samples, for $Sn_{0.95}Co_{0.025}Zn_{0.025}O_2$, a Gaussian deconvolution of the XEOL spectra (inset of Fig. 4) displays two features at ~550 nm, and the emergence of a secondary feature at ~750 nm. The primary feature at ~550 nm has similar intensity in the $Sn_{0.95}Co_{0.025}Zn_{0.025}O_2$ and the $Sn_{0.90}Co_{0.05}Zn_{0.05}O_2$ samples, but has a decreased intensity in the $Sn_{0.85}Co_{0.075}Zn_{0.075}O_2$ sample. In addition, the ~750 nm feature is seen in the $Sn_{0.95}Co_{0.025}Zn_{0.025}O_2$ but is eliminated in the $Sn_{0.90}Co_{0.05}Zn_{0.05}O_2$ and $Sn_{0.85}Co_{0.075}Zn_{0.075}O_2$ samples.

The single luminescence feature of undoped annealed SnO_2 can be attributed to inherent defects within the nanoscale material. Considering that the "as-synthesized" samples have no luminescence, and our Co and Zn L-edge measurements show that oxygen vacancies migrate from the Zn to the Co atoms, the luminescence in these systems is enabled by the migration of oxygen vacancies to a position adjacent to the cobalt atoms. Noting that the saturation magnetization of the of the x=0.05 and x=0.075 samples are two and five times greater than the x=0.025 sample, respectively, (shown in Table 1) we attribute the primary luminescence feature at 550 nm to cobalt-adjacent vacancies and the secondary feature at 750 nm to zinc-adjacent vacancies. This demonstrates that at low dopant concentrations, zinc adjacent oxygen vacancies are still present. As dopant concentration increases in the annealed $Sn_{0.90}Co_{0.05}Zn_{0.05}O_2$ and annealed $Sn_{0.85}Co_{0.075}Zn_{0.075}O_2$ samples, the elimination of the 750 nm feature suggests that zinc adjacent oxygen vacancies are no longer present, and only cobalt adjacent oxygen vacancies are contributing to the luminescence spectra.

We note that although there is no change in the nominal stoichiometry of our samples before and after annealing, in the as-synthesized samples no luminescence was observed, in contrast to the annealed samples. This can be explained by considering the differences in how the vacancies are distributed in the as-synthesized and annealed samples. In as-synthesized samples, the zinc atoms have adjacent vacancies, as seen in the Zn *L*-edge XAS experimental spectra and DFT calculations (Fig. 3). The agreement between experiment and a calculation which neglects to in-

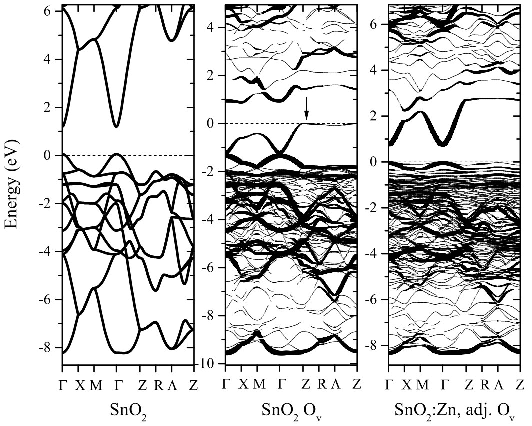

Fig. 5 Band structure diagrams of SnO$_2$, SnO$_2$ calculated for a 2x2x2 SnO$_2$ unit cell with an oxygen vacancy and a 2x2x2 SnO$_2$ unit cell with a Zinc atom with an adjacent oxygen vacancy (labeled "adj. O$_v$") for a path in the original unit cell Brillouin zone are shown in the left, middle and right panels, respectively. For the supercell band structures, the point size corresponds to the Bloch spectral weight.

clude a cobalt atom suggests high separation distance and low interaction between cobalt and zinc atoms within the host SnO$_2$ as observed in Section 3.1.1. This is in agreement with the fact that the Co *L*-edge spectra can be explained by a DFT calculated structure that does not include Zn atoms. Therefore, the relaxation of the cobalt cations into the SnO$_2$ during annealing facilitates a low interaction between cobalt and zinc atoms, and an optimal coordination for magnetic interactions.[38]

Having established the defect distribution for this system, and that the interaction between Co and Zn is weak, we are now able to explain the absence of luminescence in the as-synthesized samples by considering the band structure of SnO$_2$ with a Zn atom and an adjacent oxygen vacancy. An energy momentum diagram of SnO$_2$, a SnO$_2$ with a vacancy and SnO$_2$ with a Zn ion and an adjacent vacancy is shown in Fig. 5. In pure SnO$_2$ no mid-gap states are observed. When a vacancy is introduced, the valence band is perturbed by the addition of a dispersive mid-gap band appearing just above the top of the valence band and extending deep into the mid-gap region. The Fermi energy level is at the top of this band. Upon injecting carriers, electrons will reach a quasi-equilibrium in valleys at the bottom of the conduction band while holes will migrate to local maxima in the mid-gap band. These carriers can then recombine in momentum conserving transitions such as those indicated by an arrow in the figure. The energy-momentum diagram for Zn with an adjacent vacancy is quite different. In this case, an additional band appears at the top of the valence band, but no new mid-gap states appear, which are required to mediate luminescence in the optical region.

3.5 The connection of oxygen vacancy concentrations to magnetic properties

We find that the properties of transition-metal doped oxides are dependent on which sites transition metal ions occupy, where vacancies are distributed and their relative concentrations. The effect of concentration is demonstrated through the XEOL studies, with the presence of a secondary luminescence feature originating from zinc adjacent oxygen vacancies within annealed $Sn_{0.95}Co_{0.025}Zn_{0.025}O_2$. The disappearance of this feature in the annealed $Sn_{0.90}Co_{0.05}Zn_{0.05}O_2$ and $Sn_{0.85}Co_{0.075}Zn_{0.075}O_2$ samples and the higher saturation magnetization and exchange bias field seen in the higher dopant concentration samples demonstrates that a threshold concentration necessary for defect homogeneity within the sample.

4 Conclusions

We have investigated the local structure of Zn and Co codopants in SnO$_2$ samples with a variety of spectroscopic x-ray techniques, in addition to DFT and multiplet methodologies. We find that both Zn and Co atoms substitute for Sn atoms within the bulk of the lattice, and attribute the ferromagnetic properties to oxygen vacancy mediated substitution of Co and Zn within the host lattice. Furthermore, we identify a secondary defect state within low concentration samples only appearing after annealing that disappears with concentrations of 5% Co and 5% Zn or greater. Through this, we provide direct experimental evidence for the location and behavior of oxygen vacancies within a co-doped DMS system under annealing and connect this to observed luminescence showing the transfer of oxygen vacancies from Zn adjacent positioning pre-annealing to Co adjacent positioning post-annealing. In addition to this, the increased saturation magnetism in samples with increased dopant percentages can be attributed to the decreasing distance between Co atoms and associated cobalt-adjacent oxygen vacancies within the lattice.

The combination of synchrotron x-ray based experimental and theoretical techniques allows a link between observed magnetism and dopant–atom interactions within a host crystal. We display a novel methodology for usage of both density functional and multiplet theories for the modeling of DMS systems that proves effective in directly linking not only the existence of oxygen vacancies but the positioning of oxygen vacancies and their host lattice interactions resulting in observed ferromagnetic properties.

Conflicts of interest

There are no conflicts to declare.

Acknowledgements

This work was supported by the Natural Sciences and Engineering Research Council of Canada (NSERC) and the Canada Research Chairs program. XAS measurements were performed at the Canadian Light Source, which is supported by the Canada Foundation for Innovation, Natural Sciences and Engineering Research Council of Canada, the University of Saskatchewan, the Government of Saskatchewan, Western Economic Diversification Canada, the National Research Council Canada, and the Canadian Institutes of Health Research. RXES measurements were performed at the Advanced Light Source, which is supported by the US Department of Energy under Contract No. DE-AC02-05CH11231. We are grateful for the use of the Plato computing cluster at the University of Saskatchewan and this research was enabled in part by support provided by Westgrid and Compute Canada.

Notes and references

1 S. A. Wolf, D. D. Awschalom, R. A. Buhrman, J. M. Daughton, S. v. Molnár, M. L. Roukes, A. Y. Chtchelkanova and D. M. Treger, *Science*, 2001, **294**, 1488–1495.

2 T. Dietl, *Nat. Mater.*, 2003, **2**, 646–648.

3 H. Ohno, *Science*, 1998, **281**, 951–956.

4 K. Nomura, J. Okabayashi, K. Okamura and Y. Yamada, *J. Appl. Phys.*, 2011, **110**, 83901.

5 J. Kaur, J. Shah, R. Kotnala and K. C. Verma, *Ceram. Int.*, 2012, **38**, 5563–5570.

6 S. Ghosh, G. G. Khan and K. Mandal, *ACS Appl. Mater. Interfaces*, 2012, **4**, 2048–2056.

7 J. Hays, A. Punnoose, R. Baldner, M. H. Engelhard, J. Peloquin and K. M. Reddy, *Phys. Rev. B*, 2005, **72**, 75203.

8 S. J. Potashnik, K. C. Ku, S. H. Chun, J. J. Berry, N. Samarth and P. Schiffer, *Appl. Phys. Lett.*, 2001, **79**, 1495–1497.

9 E. T. Selvi and S. M. Sundar, *Appl. Phys. A*, 2017, **123**, 383.

10 Y. Fu, N. Sun, L. Feng, S. Wen, Y. An and J. Liu, *J. Alloys and Compd.*, 2017, **698**, 863–867.

11 M. García-Tecedor, D. Maestre, A. Cremades and J. Piqueras, *J. Phys. Chem. C*, 2016, **120**, 22028–22034.

12 X. Liu, J. Iqbal, Z. Wu, B. He and R. Yu, *J. Phys. Chem. C*, 2010, **114**, 4790–4796.

13 J. Okabayashi, S. Kono, Y. Yamada and K. Nomura, *J. Appl. Phys.*, 2012, **112**, 73917.

14 H. Katayama-Yoshida, T. Nishimatsu, T. Yamamoto and N. Orita, *J. Phys.: Condens. Matter*, 2001, **13**, 8901.

15 D. Manikandan and R. Murugan, *Superlattices and Microstructures*, 2016, **89**, 7–14.

16 V. B. Kamble, S. V. Bhat and A. M. Umarji, *Journal of Applied Physics*, 2013, **113**, 244307.

17 R. Khan, Zulfiqar, S. Fashu and Y. Zaman, *Journal of Materials Science: Materials in Electronics*, 2016, **27**, 5960–5966.

18 K. Rajwali and M.-H. Fang, *Chinese Physics B*, 2015, **24**, 127803.

19 R. Khan, Zulfiqar, M. U. Rahman and S. Fashu, *Journal of Materials Science: Materials in Electronics*, 2017, **28**, 2673–2679.

20 M. Boots, D. Muir and A. Moewes, *J Synchrotron Radiat.*, 2013, **20**, 272–285.

21 R. Qiao, Q. Li, Z. Zhuo, S. Sallis, O. Fuchs, M. Blum, L. Weinhardt, C. Heske, J. Pepper, M. Jones, A. Brown, A. Spucces, K. Chow, B. Smith, P.-A. Glans, Y. Chen, S. Yan, F. Pan, L. F. J. Piper, J. Denlinger, J. Guo, Z. Hussain, Y.-D. Chuang and W. Yang, *Review of Scientific Instruments*, 2017, **88**, 33106.

22 T. Regier, J. Krochak, T. K. Sham, Y. F. Hu, J. Thompson and R. I. R. Blyth, *Nucl. Instrum. Methods Phys. Res., Sect. A*, 2007, **582**, 93–95.

23 K. Schwarz and P. Blaha, *Comput. Mater. Sci*, 2003, **28**, 259–273.

24 J. Perdew, A. Ruzsinszky, G. Csonka, O. Vydrov, G. Scuseria, L. Constantin, X. Zhou and K. Burke, *Phys. Rev. Lett.*, 2008, **100**, 136406.

25 F. Tran, J. Stelzl and P. Blaha, *The Journal of Chemical Physics*, 2016, **144**, 204120.

26 G.-X. Zhang, A. M. Reilly, A. Tkatchenko and M. Scheffler, *New Journal of Physics*, 2018, **20**, 063020.

27 A. A. Bolzan, C. Fong, B. J. Kennedy and C. J. Howard, *Acta Crystallogr., Sect. B*, 2007, **53**, 373–380.

28 K. Schwarz, A. Neckel and J. Nordgren, *J. Phys. F: Met. Phys.*, 1979, **9**, 2509.

29 Y. Hinuma, G. Pizzi, Y. Kumagai, F. Oba and I. Tanaka, *Comput. Mater. Sci*, 2017, **128**, 140–184.

30 O. Rubel, A. Bokhanchuk, S. J. Ahmed and E. Assmann, *Phys. Rev. B*, 2014, **90**, 115202.

31 E. Antonides, E. C. Janse and G. A. Sawatzky, *Phys. Rev. B*, 1977, **15**, 1669–1679.

32 R. D. Cowan, *J. Opt. Soc. Am.*, 1968, **58**, 808–818.

33 M. Haverkort, G. Sangiovanni, P. Hansmann, A. Toschi, Y. Lu and S. Macke, *Europhys. Lett.*, 2014, **108**, 57004.

34 M. Haverkort, *Ph.D. Thesis, University of Cologne*, University of Cologne, 2005.

35 H. Wang, Y. Yan, Y. S. Mohammed, X. Du, K. Li and H. Jin, *J. Magn. Magn. Mater.*, 2009, **321**, 337–342.

36 E. Z. Kurmaev, R. G. Wilks, A. Moewes, L. D. Finkelstein, S. N. Shamin and J. Kuneš, *Phys. Rev. B*, 2008, **77**, 165127.

37 X. T. Zhou, J. G. Zhou, M. W. Murphy, J. Y. P. Ko, F. Heigl, T. Regier, R. I. R. Blyth and T. K. Sham, *The Journal of Chemical Physics*, 2008, **128**, 144703.

38 I. Djerdj, Z. Jagličić, D. Arčon and M. Niederberger, *Nanoscale*, 2010, **2**, 1096–1104.